The Astrophysical Journal Letters, 895:L7 (7pp), 2020 May 20 https://doi.org/10.3847/2041-8213/ab8e35

3D Numerical Simulation of Kink-driven Rayleigh–Taylor Instability Leading to Fast Magnetic Reconnection

Pakorn Wongwaitayakornkul[1], Hui Li[2], and Paul M. Bellan[1]
[1] Applied Physics and Materials Science, California Institute of Technology, Pasadena, CA 91125, USA; pwongwai@ucsd.edu
[2] Theoretical Division, Los Alamos National Laboratory, Mail Stop B227, Los Alamos, NM 87545, USA
Received 2020 February 20; revised 2020 April 27; accepted 2020 April 28; published 2020 May 18

Abstract

Fast magnetic reconnection involving non-MHD microscale physics is believed to underlie both solar eruptions and laboratory plasma current disruptions. While there is extensive research on both the MHD macroscale physics and the non-MHD microscale physics, the process by which large-scale MHD couples to the microscale physics is not well understood. An MHD instability cascade from a kink to a secondary Rayleigh–Taylor instability in the Caltech astrophysical jet laboratory experiment provides new insights into this coupling and motivates a 3D numerical simulation of this transition from large to small scale. A critical finding from the simulation is that the axial magnetic field inside the current-carrying dense plasma must exceed the field outside. In addition, the simulation verifies a theoretical prediction and experimental observation that, depending on the strength of the effective gravity produced by the primary kink instability, the secondary instability can be Rayleigh–Taylor or mini-kink. Finally, it is shown that the kink-driven Rayleigh–Taylor instability generates a localized electric field sufficiently strong to accelerate electrons to very high energy.

Unified Astronomy Thesaurus concepts: Magnetohydrodynamical simulations (1966); Magnetohydrodynamics (1964); Laboratory astrophysics (2004); Experimental models (2098); Plasma astrophysics (1261)

1. Introduction

Plasma stability has long been a subject of great interest in many situations. As notable examples, a stable plasma is essential to achieve nuclear fusion and, in the solar corona, plasma instabilities are considered to be the cause for energetic phenomena. Bernstein et al. (1958) were the first to study ideal magnetohydrodynamic (MHD) stability of plasma via the MHD energy principle that states that if a perturbation lowers the total potential energy of a non-dissipative (ideal) MHD plasma, the perturbation is unstable. The energy principle involves assuming a small displacement from an initial equilibrium, then deriving linearized equations formulated as a normal-mode eigenvalue problem, and finally showing that plasmas governed by ideal MHD are susceptible to two distinct types of instabilities, denoted as pressure-driven and current-driven. A common example of pressure-driven instability, the Rayleigh–Taylor instability (RTI; Strutt 1883; Taylor 1950; Kruskal & Schwarzschild 1954), takes place at the interface between a heavy fluid sitting on top of a light fluid in a gravitational field. A common example of current-driven instability, the kink instability (KI; Kruskal et al. 1958; Shafranov 1958; Suydam 1958), involves a flux rope with an initially straight axis having the axis become helical (writhing of flux rope) so as to lower overall magnetic energy and tend toward a force-free state. Both the KI (Rust & LaBonte 2005) and the RTI (Carlyle et al. 2014) have been observed in the solar corona.

Magnetic reconnection, a microscopic instability involving physics beyond ideal MHD, is thought to be responsible for many solar eruptive events such as flares and coronal mass ejections. The simplest reconnection model is based on taking into account finite resistivity in MHD and was proposed by Sweet (1958), Parker (1957), and Furth et al. (1963). However, the predicted rate for this "resistive" reconnection is far too slow to describe actual solar eruptive events and many laboratory plasma reconnection observations, so a more sophisticated, faster microscopic model is needed. Models for fast reconnection are the subject of much ongoing research (Drake et al. 2008; Yamada et al. 2010; Eyink et al. 2011; Yoon & Bellan 2019) and typically involve microscopic physics beyond the scope of resistive MHD. This fast reconnection physics involves finite ion skin depth, finite electron inertia, and Hall terms, all of which are small scale and omitted from MHD. However, it is unclear how MHD, a macroscopic description, couples to the microscopic non-MHD scale where fast reconnection occurs.

The Caltech astrophysical jet experiment (Bellan 2018a) has provided some insights into this coupling because both the macroscopic MHD scale and the microscopic non-MHD scale can be resolved. An MHD-driven dense plasma jet is created in this experiment by a coaxial magnetized plasma gun located inside a large cylindrical vacuum chamber. The motion is described using a cylindrical coordinate system $\{r, \theta, z\}$ where the z-axis is along the vacuum chamber axis, the r, z directions are denoted poloidal, and the θ direction is denoted toroidal. The sequence of operation starts with the establishment of a dipole-shape bias poloidal magnetic field (peak value $\sim$0.1 T). Neutral gas is then injected into the vacuum chamber using fast gas valves connected to discrete nozzles located on coaxial disk and annulus electrodes at $z = 0$. After gas injection, a high voltage (3–5 kV) is applied across the electrodes from a capacitor bank to breakdown the gas to form plasma. The capacitor discharge ramps up 50–150 kA current that flows along poloidal magnetic field flux surfaces and produces an associated toroidal magnetic field. Magnetic forces associated with this current squeeze together poloidal flux surfaces radially and distend these surfaces axially so plasma frozen to these flux surfaces collimates and becomes a $\sim$40 km s^{-1} jet that propagates in the z direction from the electrodes into the chamber. The jet lasts about 20 μs and its flow and collimation agree with predictions based on detailed analytical and

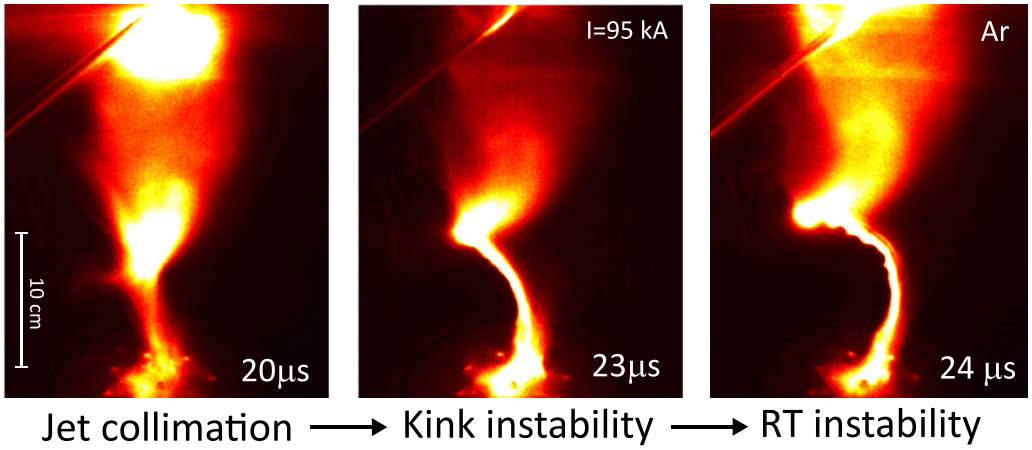

Figure 1. Evolution of KDRT instability on the argon plasma jet (shot#11,225) shows the development at 24 μs of a set of RTI ripples on the inner (trailing) side of a helical kink. The white label indicates the time after the plasma breakdown.

numerical consideration of MHD forces (Kumar & Bellan 2009; Yun & Bellan 2010; Zhai et al. 2014; Bellan 2018a, 2018b). The jet formation, collimation, and axial lengthening have been observed using a fast movie camera. Hsu & Bellan (2003) observed a clear KI using the fast movie camera while Moser & Bellan (2012) detected a secondary RTI that happened on the inner (trailing) side of the KI. The KI growth means that the plasma jet moves laterally from the z-axis with exponentially increasing displacement and so undergoes a large lateral acceleration perpendicular to the z-axis. In the frame of this laterally accelerating plasma, the system of heavy fluid (plasma) and light fluid (vacuum) thus experience a strong ($\sim 10^{10}\,\mathrm{m\,s^{-2}}$) effective gravity g pointing toward the z-axis. As seen in Figure 1 the kink-driven Rayleigh–Taylor instability (KDRT) occurs on the trailing side of the KI corresponding to the dense plasma being "on top of" the diffuse external region. The timescale of the RTI is about 3× shorter than the KI timescale so the two instabilities are decoupled other than the KI providing the effective gravity g. The minor radius of the current-carrying flux rope decreases with spatial periodicity as a result of the choking effect of the RTI ripples. Fast reconnection takes place when the flux rope is choked to a radius comparable to the ion skin depth $d_i = c/\omega_{\mathrm{pi}}$. When this happens several simultaneous phenomena occur, namely, a strong localized EUV emission (Chai et al. 2016), a strong localized reduction of visible light, a voltage spike, a hard X-ray burst (Marshall et al. 2018), and a whistler wave burst (Haw et al. 2019). These non-MHD phenomena indicate that the choking of the jet radius by the KDRT is the macroscopic ideal MHD mechanism that allows the initially MHD-governed plasma to access the microscopic d_i length scale where fast reconnection occurs.

While extensive numerical studies of both KI (Linton et al. 1996; Török & Kliem 2005; Bergerson et al. 2006) and RTI (Youngs 1984, 1991) individually exist, no numerical simulation of KDRT has been demonstrated. Since the lab experiments indicate that KDRT provides a cascade path from macroscopic ideal MHD to microscopic fast reconnection, it is likely that KDRT can also explain many energetic events observed in nature. This suggests that a numerical simulation would be extremely valuable and could be checked against the experiment and existing analytic models. For example, Zhai & Bellan (2016) proposed a quantitative analytic model for how lateral acceleration of a cylindrical current-carrying plasma could result in either RTI or a mini-kink depending on the ratio of lateral gravitational acceleration to the pinch force resulting from the current. However, this model did not arrange for the lateral acceleration to be from a primary KI and there was no numerical simulation showing the RTI being driven by a KI. Similarly, a statistical model of electron acceleration from a reconnecting electric field was developed (Marshall & Bellan 2019), but there was no numerical verification using actual geometry.

Simulating the KDRT numerically poses many challenges. First, the code must include finite β, since the equilibrium preceding the RTI involves a balance between magnetic and hydrodynamic pressure. Equally important, there must be a density jump or gradient to have a heavy fluid on top of a light fluid when the effective gravity is developed by the KI. Second, the code has to capture the instability in full 3D at high resolution because multiple length scales are involved and because the KI and RTI are fundamentally three-dimensional as they involve a writhing flux rope. The code also has to resolve three different timescales, namely, the jet collimation timescale (τ_{col}), the KI timescale (τ_{kink}), and the RTI timescale (τ_{RT}), where $\tau_{\mathrm{col}} \gg \tau_{\mathrm{kink}} \gg \tau_{\mathrm{RT}}$.

We report here 3D numerical simulation of the KDRT. This simulation, achieved using resistive MHD, is in good agreement with the experimental observations and also with the predictions of Zhai & Bellan (2016) regarding the secondary instability being either RTI or mini-kink. Section 2 describes the simulation model by presenting the system of equations and the initial and boundary conditions. Section 3 discusses the circumstances leading to KDRT and specifically shows that spatial localization of the axial magnetic field B_z is a key requirement. This localization is achieved experimentally via the collimation process and corresponds to the jet being paramagnetic (Li & Cross 1994). Section 4 numerically validates the analytic results predicted by Zhai & Bellan (2016), showing that the secondary instability could be either RTI or mini-kink depending on the dimensionless parameter $\Phi^2 = ga/v_{\mathrm{A}\theta}^2$, where a is the flux rope radius and $v_{A\theta}$ is an Alfvén velocity calculated using B_θ only, serving as a measure of the pinch force. Section 5 discusses the assumptions made regarding resistivity and the acceleration of test particles injected into a resistive MHD plasma; this section shows that particles will be accelerated to high energy when there is a localized anomalous resistivity imposed as a proxy for the

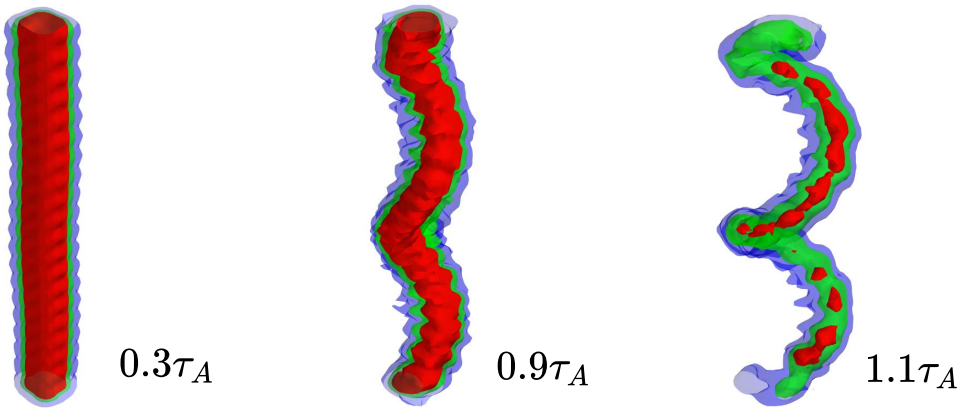

Figure 2. Simulated KDRT at three different time steps. τ_A is the Alfvén time of the simulation. The isosurfaces represent $\{0.2\rho_0, 0.3\rho_0, 0.4\rho_0\}$ with blue, green, and red, respectively.

microphysics associated with fast magnetic reconnection. Section 6 relates the simulation to the laboratory observations and the possible applicability of the simulation to the solar corona.

2. 3D Resistive MHD Simulation

The 3D MHD numerical simulation was performed on the Los Alamos Turquoise supercomputer cluster using part of the Los Alamos COMPutational Astrophysical Simulation Suite (Li & Li 2003), which is a collection of several high-resolution, Godunov-type, MHD codes. This suite had been previously used to model the Caltech astrophysical jet and solar loop experiments (Zhai et al. 2014; Wongwaitayakornkul et al. 2017). An important difference here is that a spatially and temporally dependent finite resistivity is included. The initial situation is a flux rope (finite radius cylinder with helical magnetic field and embedded finite density plasma) surrounded by extremely low density plasma. The code tracks the evolution of eight dimensionless parameters, namely, density ρ, velocity $\boldsymbol{v}$, magnetic field $\boldsymbol{B}$, and pressure P inside a Cartesian box of size $[-L, L]^3$ where $L = 10a$ and, as before, a is the flux rope initial radius. The domain box contains 80^3 meshes. The dimensionless parameters are obtained by normalizing to associated dimensioned reference parameters. These reference parameters are the azimuthal magnetic field just outside the plasma column $B_0 = B_\theta(r = a)$, the initial density on the flux rope axis $\rho_0 = \rho(r = 0)$, the domain half-length L, the Alfvén velocity associated with the azimuthal magnetic field $v_A = B_0/\sqrt{\mu_0\rho_0}$, the Alfvén time $\tau_A = L/v_A$, the initial on-axis pressure $p_0 = \rho_0 v_A^2$, and the initial hydrodynamic energy $p_0 L^3$. The Lundquist number is defined as $S = \mu_0 v_A L/\eta$.

The code solves the dimensionless resistive MHD equations in conservative form, namely,

$$\frac{\partial \rho}{\partial t} + \nabla \cdot (\rho \boldsymbol{v}) = 0, \tag{1}$$

$$\frac{\partial (\rho \boldsymbol{v})}{\partial t} + \nabla \cdot \left(\rho \boldsymbol{v}\boldsymbol{v} + \left(P + \frac{B^2}{2} \right) \overleftrightarrow{\boldsymbol{I}} - \boldsymbol{B}\boldsymbol{B} \right) = 0, \tag{2}$$

$$\frac{\partial e}{\partial t} + \nabla \cdot \left[\left(e + P + \frac{B^2}{2} \right) \boldsymbol{v} - \boldsymbol{B}(\boldsymbol{v} \cdot \boldsymbol{B}) \right] = 0, \tag{3}$$

$$\frac{\partial \boldsymbol{B}}{\partial t} - \nabla \times (\boldsymbol{v} \times \boldsymbol{B}) - \frac{1}{S} \nabla^2 \boldsymbol{B} = 0, \tag{4}$$

where the total energy density is $e \equiv \rho v^2/2 + P/(\gamma - 1) + B^2/2$ with $\gamma = 5/3$. The initial condition is that of an axisymmetric flux rope with uniform axial current density $J_z = I/(\pi a^2)$ for $r < a$ and $J_z = 0$ for $r > a$. In one configuration (extreme paramagnetism) a uniform axial magnetic field B_z exists only inside the current channel ($r < a$) while in another configuration B_z exists over the entire domain. The code evolves the vector potential $\boldsymbol{A} = (A_x, A_y, A_z)$ to maintain the divergenceless condition of the magnetic field, $\nabla \cdot \boldsymbol{B} = 0$. The density is set to have a Gaussian profile that decays radially from the flux rope axis that is located at position $\boldsymbol{r}_0$. A small uniform background density ρ_b was added to avoid requiring an infinitely small time step. The plasma is initially at rest with a uniform temperature, $T = P/\rho = 1$. The initial density, pressure, velocity, and vector potential are specified as

$$\rho = \rho_0 \exp\left(-(\boldsymbol{r} - \boldsymbol{r}_0)^2/2\sigma^2\right) + \rho_b, \tag{5}$$

$$P = \rho, \boldsymbol{v} = 0, A_x = 0, A_y = B_z x, \tag{6}$$

$$A_z = \begin{cases} -(I/4\pi)(r/a)^2, & r < a \\ -(I/4\pi)(1 + 2\ln(r/a), & r > a \end{cases}, \tag{7}$$

where $\rho_0 = 1$, $\boldsymbol{r}_0 = 0$, $\rho_b = 0.01$, $\sigma = 0.1$, $I = 1$, $a = 0.1$, and $B_z = 0.3$. For the paramagnetic configuration B_z is finite inside the flux rope ($r < a$) only. The parameters are chosen so that $P(r = 0) \sim B_\theta(r = a)^2/2$ and the flux rope is in approximate radial equilibrium since $B_z \ll B_\theta$. Resistivity is set to zero ($\eta = 0$) in Sections 3–4 but then is set to be finite and spatially dependent in Section 5.1. Seed perturbations for both KI and RTI are added to the initial state by setting $\boldsymbol{r}_0 = \sin(2\pi z/\lambda_{\rm KI})\hat{\imath} + \cos(2\pi z/\lambda_{\rm KI})\hat{\jmath}$ to provide a KI seed, and by setting $\sigma = a(1 + 0.1\sin(2\pi z/\lambda_{\rm RTI}))$ to provide a RTI seed. The seed perturbations have $\lambda_{\rm RTI} = 0.1$ and $\lambda_{\rm KI} = 1$. Spatial boundary conditions are current-conserving non-reflecting outflow at the bounding surfaces.

Figure 2 shows the time evolution of the numerical simulation. On the left ($t = 0.3\tau_A$), the plasma is initially in a near straight cylinder equilibrium with the small KI and RTI seed perturbations visible. The KI takes place on the Alfvén timescale and so appears at $t = 0.9\tau_A$ (middle in Figure 2). The lateral acceleration of the kink produces the effective gravity that sets off the RTI that grows on a much shorter timescale

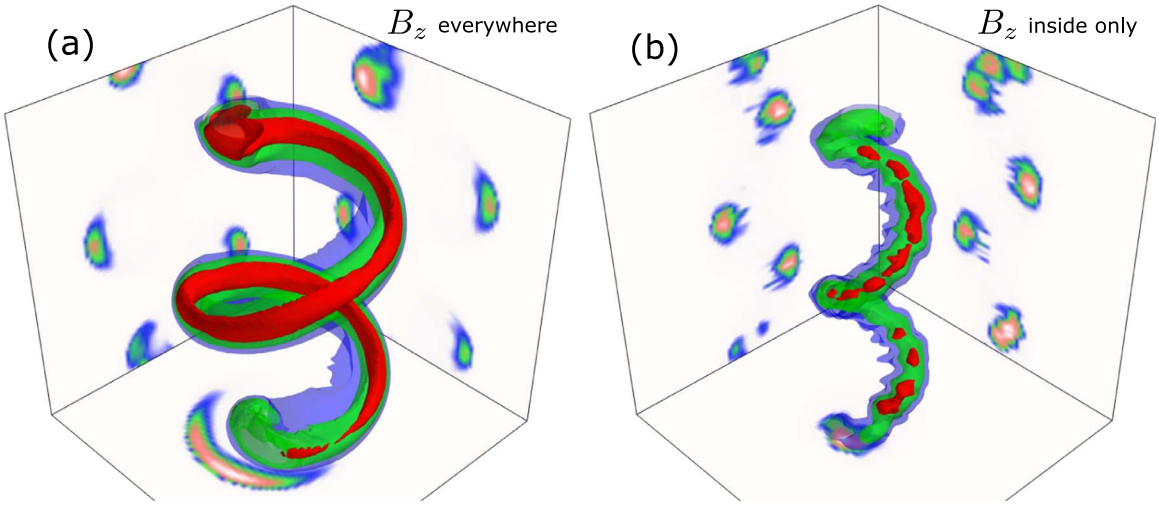

Figure 3. Isosurfaces snapshot of density in two cases: (a) with uniform $B_z = 0.3$ and (b) with $B_z = 0.3$ only inside the flux rope ($r < a$). Both cases are taken at the same time $t = 1.1\ \tau_A$. The colors blue, green, and red indicate the levels {0.5, 0.7, 0.9} of the maximum density of that time frame accordingly. The planes show a cross-sectional contour of the density in the midplane.

($\sim 0.2\tau_A$). The density isosurfaces at $t = 1.1\tau_A$ show that the RTI has approximately e-folded and has the same short wavelength as the RTI seed perturbation.

On using imputed experimental parameters $n_0 = 10^{23}\,\mathrm{m}^{-3}$, $B_0 = 1.9$ T, $L = 10$ cm, $\kappa T = 2$ eV, and $m_i = 40$ u (Ar), it follows that $v_A = 20\,\mathrm{km\,s}^{-1}$ and $\tau_A = 5\ \mu$s. The predicted timescale for each process matches well with the observed timescale, i.e., $\tau_{\mathrm{col}} = 2\tau_A \rightarrow 10\ \mu$s, $\tau_{\mathrm{kink}} = 0.9\tau_A - 0.3\tau_A = 0.6\tau_A \rightarrow 3\ \mu$s, and $\tau_{\mathrm{RT}} = 1.1\tau_A - 0.9\tau_A = 0.2\tau_A \rightarrow 1\ \mu$s where the arrow represents converting the dimensionless quantity to its associated dimensioned value. The word "imputed" is used here because the minor radius of 1 cm is too small for a magnetic probe measurement and the kink dynamics is too fast and unpredictable for a density interferometer measurement.

3. Conditions for KDRT

As demonstrated in Figure 3, the simulation shows that B_z must be localized in the flux rope for the kink-driven RTI to develop. Having B_z much larger inside the flux rope than outside corresponds to the flux rope being highly paramagnetic (Li & Cross 1994). Figure 3 compares the localized B_z case (i.e., paramagnetic) to the case where B_z exists everywhere. In Figure 3(a), B_z is applied everywhere in the domain, while in Figure 3(b), B_z is finite only inside the flux rope. Even though all other parameters are identical, KDRT is only observed when B_z is localized to be inside the flux rope. This paramagnetic situation corresponds to the natural state of the experiment because the jet collimation process squeezes together axial magnetic field lines that were initially spread apart (Hsu & Bellan 2003). Since magnetic field strength is just the density of field lines, the squeezed together field lines are by definition paramagnetic. This nonuniformity and paramagnetism is also expected in the solar corona context because the collimation of solar flux ropes similarly requires the gathering together of axial magnetic field lines that were initially spread apart (Klimchuk 2001).

This requirement for axial magnetic field paramagnetism demonstrated in Figure 3 suggests that the axial magnetic field outside the flux rope has a stabilizing effect and inhibits the RT ripples from developing. An analytical growth rate of the RTI in a slab geometry on an interface between a plasma with density ρ and a vacuum is

$$\gamma = gk - \alpha\frac{(\boldsymbol{k}\cdot\boldsymbol{B})^2}{\mu_0\rho}, \tag{8}$$

where g is a gravitational acceleration, k is the RTI wavenumber, and $\boldsymbol{B}$ is a magnetic field parallel to the interface. $\alpha = 1$ when this magnetic field is present on only one side of the interface and $\alpha = 2$ when this magnetic field is present on both sides (Goedbloed et al. 2019, Section 6.6.4). The predicted growth rate is smaller when $\alpha = 2$, so the uniform magnetic field across the interface provides a stronger stabilization to the instability. Although the RTI developed here is for a cylindrical geometry, the stabilizing trend should also apply to an RTI developed in a slab geometry.

4. Effect on Φ^2

As the plasma undergoes the kink instability, a large effective gravity is established in the frame of the plasma. The Rayleigh–Taylor instability develops on the inner side of the flux rope as it involves a system of heavy fluid (plasma) on top of a light fluid (vacuum). From the simulation run in Figure 3(b), the gravitational acceleration established by the kink instability is $\bar{g} = 1.5 \rightarrow 6 \times 10^9\ \mathrm{m\ s}^{-2}$; this number matches well the experimentally observed value (Moser & Bellan 2012; Zhai & Bellan 2016). If the plasma travels 5 cm in $\tau_{\mathrm{kink}} = 3\ \mu$s, then the acceleration is $5\,\mathrm{cm}/(3\ \mu\mathrm{s})^2 = 6 \times 10^9\ \mathrm{m\,s}^{-2}$. The acceleration is significant and the limit in which this effective gravitational field will be important to the development of RTI is investigated in this section.

Zhai & Bellan (2016) proposed that, under certain conditions, a current-carrying flux rope immersed in a gravitational field should exhibit an instability intermediate between current-driven and pressure-driven. This hybrid instability depended on a cross-coupling between members of the broad spectrum of azimuthal modes required to accommodate both the Cartesian geometry $\{x, y, z\}$ of lateral gravity and the cylindrical geometry $\{r, \theta, z\}$ of a flux rope. This situation is both more complicated and more realistic than the traditional Cartesian model of the RTI and the traditional cylindrical model of the KI. Zhai & Bellan (2016) defined a dimensionless parameter

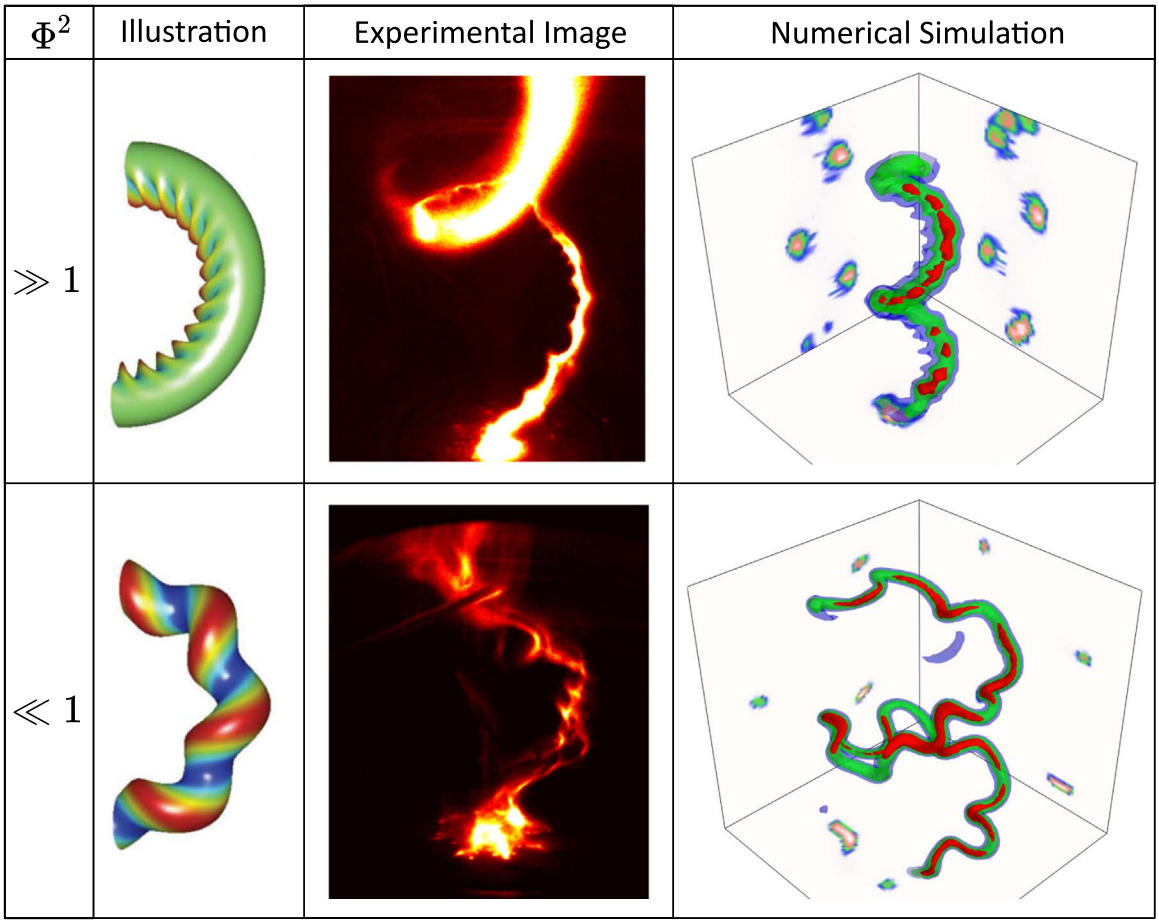

Figure 4. The two limits of the instability are shown: (a) $\Phi^2 \gg 1$ and (b) $\Phi^2 \ll 1$. The instability is shown in the Illustration column, where the shape of the instability is calculated analytically. Second, the different regimes are captured with a fast camera. The right-hand column shows the 3D numerical simulation. The numerical plots are isosurfaces of density. The figures in the Illustration and Experimental Image columns are adapted from Zhai & Bellan (2016). The Numerical Simulation column is the result of this work.

$\Phi^2 = ga/v_{A\theta}^2$ where $v_{A\theta} = B_0/\sqrt{\mu_0\rho_0}$ and showed that if $\Phi^2 \gg 1$ the flux rope was more susceptible to RTI and if $\Phi^2 \ll 1$ the flux rope was more susceptible to KI. Figure 4 compares the Φ^2 regimes for the analytic solution, the experiment, and the 3D MHD numerical simulation (the analytic solution and experiment are from Zhai & Bellan 2016 and the 3D numerical solution is the new result presented here). In the illustration column, two curved flux ropes are shown. The upper row shows a flux rope with $\Phi^2 \gg 1$, the RTI-dominated case, while the lower row shows a flux rope with $\Phi^2 \ll 1$, the KI dominated case. The parameter Φ^2 can be expressed as $\Phi^2 = ga/v_{A\theta}^2 = \mu_0\rho ga/B_\theta^2 = \mu_0 m_i n_i ga/B_\theta^2$. In the experiment (Zhai & Bellan 2016), the two cases ($\Phi^2 \gg 1$ and $\Phi^2 \ll 1$) have comparable g, a, B_θ, and n_i. The difference in value of Φ^2 comes from ion mass: argon ($m_i = 40$ u) is used in the $\Phi^2 \gg 1$ case and hydrogen ($m_i = 1$ u) is used in the $\Phi^2 \ll 1$ case. In the simulation, the normalization constant for temperature is defined as $\kappa T_0 = m_i P_0/\rho_0$. Therefore, lowering m_i is equivalent to lowering T_0 while keeping the other parameters fixed. Increasing the pressure, while maintaining the plasma density, increases the numerical value of the temperature. Suppose in the experiment the temperature of both argon and hydrogen plasma are the same ($\kappa T \sim 2$ eV), varying the background pressure p_b is equivalent to varying m_i in the experiment. Consequently, Φ^2 can be tuned by changing m_i in the experiment and p_b in the simulation. In the simulation column of Figure 4, $p_b = 10^{-4}$ in the upper row and $p_b = 1$ in the lower row.

5. Electron Acceleration

Theoretical investigations (e.g., Chen & Wu 2012) have shown that microphysical kinetic Alfvén wave instabilities are triggered when the electron drift velocity relative to ions, i.e., $v_d = J/ne$, exceeds the Alfvén velocity. When this happens, electrons are scattered by the microscopic wave turbulence leading to a reduction in directed electron momentum and hence an increase in the effective plasma resistivity. This section addresses the effect of this "anomalous" resistivity. Section 5.1 describes how such an anomalous resistivity affects the MHD simulation; the anomalous resistivity η is switched on in the region where v_d exceeds some threshold. Section 5.2 describes the trajectory of test electrons in the presence of the simulation magnetic field and the electric field created by the anomalous resistivity. Because the test electrons have very fast trajectories, we assume the plasma does not change when calculating these trajectories. The justification for this "frozen plasma" assumption is that the cyclotron period is $\tau_c = 2\pi m_e/eB_0$ and the electron thermal speed is $v_T = \sqrt{2\kappa T/m_e}$ so $\tau_A/\tau_c = eL\sqrt{\mu_0 m_i n_i}/2\pi m_e = 2.6 \times 10^5$ and $v_T/v_A = \sqrt{2\kappa T\mu_0 m_i n_i/m_e}/B_0 = 40$. On defining the test electron transit time $\tau_T = L/v_T$, it is seen that $\tau_A/\tau_T \gg 1$. Initially, the ion skin depth $d_i = (c/e)\sqrt{\epsilon_0 m_i/n} = 0.5$ cm $< a$. Then, KDRT chokes down the current

cross-section to be below d_i prompting fast reconnection. Using electron drift velocity $v_d = J/(ne) = 2B_\theta/(\mu_0 ane)$ and Alfvén velocity $v_A = B/\sqrt{\mu_0\rho} = \sqrt{2(B_\theta^2 + B_z^2)}/(\mu_0 m_i n)$, we can express the ratio between the two velocities as $v_d/v_A = (d_i/a)\sqrt{2/(1 + (B_z/B_\theta)^2)}$. Therefore, for $B_z \leqslant B_\theta$, $d_i/a \sim \mathcal{O}(1)$ corresponds to $v_d/v_A \sim \mathcal{O}(1)$ and squeezing the plasma radius to the ion skin depth corresponds to the electron drift velocity becoming of the order the Alfvén velocity, which is kinetically unstable.

5.1. Anomalous Resistivity

Fast reconnection occurs at the microscopic d_i scale when non-MHD kinetic physics becomes important and the concept of resistivity is an oversimplification. Because of the complexity of the microscale physics, it is not computationally feasible to describe these effects in correct detail in a code that also describes the 3D MHD physics. However, by making some simplifying physical arguments (Wilkins 1980) one can gain insights into the effect of the microphysics. These arguments consist of adding a large ad hoc localized anomalous resistivity to the 3D MHD code. While this addition does not accurately describe the microphysics of the fast magnetic reconnection, it does give insight into the accelerating process of the electrons.

The condition to trigger the ad hoc anomalous localized resistivity η_a is for the current density J to exceed a certain threshold J_c. This is quantitatively expressed as

$$\eta(J, t) = \eta_a H(J - J_c) H(t - t_c), \tag{9}$$

where $\eta_a = \mu_0 L v_A/S_a$ is the normalized anomalous resistivity, S_a is the anomalous Lundquist number, J_c and t_c are the critical current density and time at which microphysics kinetic instabilities are triggered, and H is the Heaviside step function. The normalization constant for J_c is $J_0 = B_0/\mu_0 L = 1.4 \times 10^7\ \mathrm{A\ m^{-2}}$. Using the Caltech jet parameters where 6 keV X-rays are observed (Marshall et al. 2018) in association with RTI we assume an electron is accelerated to 6 keV in 1 cm. This implies the existence of a localized parallel electric field $E_\parallel = 6 \times 10^5\ \mathrm{V\ m^{-1}}$. We choose $J_c = 15$ and $t_c = 1.2$ so that the large resistivity is turned on at the same time and locations as the reconnection event in the experiment. This defines $\eta_a \equiv E_\parallel/J_c$ and implies $S_a = 1.0$. In addition to a J-dependent factor, a time-dependent factor is included to properly trigger the reconnection due to the discrepancy between the boundary conditions in the simulation and experiment.

5.2. Particle Simulation

The trajectory of test electrons is calculated using a snapshot of the MHD simulation with a localized parallel electric field provided by the anomalous resistivity. Figure 5 shows the contour of the parallel electric field $E_\parallel = \eta \boldsymbol{J} \cdot \boldsymbol{B}/B$. The guiding center approximation (Northrop 1961) is used to describe the test electron motion.

$$\frac{\mathrm{d}u_\parallel}{\mathrm{d}t} = \frac{q}{m}E_\parallel - \frac{\mu}{mB}(\boldsymbol{B} \cdot \nabla)B, \tag{10}$$

$$\frac{\mathrm{d}\boldsymbol{r}}{\mathrm{d}t} = \frac{u_\parallel}{B}\boldsymbol{B} + \frac{\boldsymbol{E} \times \boldsymbol{B}}{B^2} + \frac{\mu}{qB^2}\boldsymbol{B} \times \nabla B + \frac{mu_\parallel^2}{qB^4}\boldsymbol{B} \times (\boldsymbol{B} \cdot \nabla)\boldsymbol{B}, \tag{11}$$

where $\mu = mu_\perp^2/2B =$ constant. The parallel electric field is generated at the location of high current density where the anomalous resistivity is turned on via Equation (9). From the simulation, we measure $E_\parallel = 6 \times 10^5\ \mathrm{V\ m^{-1}}$. The electrons have an initial thermal speed $v_T = \sqrt{2kT/m_e}$. For $\kappa T = 2$ eV, $n = 10^{23}\ \mathrm{m^{-3}}$, $m_i = 40$ u, $B_0 = 1.9$ T, and $v_T/v_A = \sqrt{2\kappa T \mu_0 m_i n_i/m_e}/B_0 = 40$. The initial pitch angles are chosen at random and the initial positions are (x_p, y_p, z_p). The 1000 particles are randomly placed inside a cube defined by $-0.2 \leqslant x_p \leqslant 0.0$, $-0.4 \leqslant y_p \leqslant -0.2$, $-0.5 \leqslant z_p \leqslant -0.3$; this cube is shown by black lines in Figure 5(a).

The red lines in Figure 5(a) show the trajectory of particles that are accelerated to high energy on passing through the large resistive region. The other non-accelerated particles are indicated by gray lines. The particle energy distribution, shown in Figure 5(b), indicates that 10% of the particles are accelerated to energy above 1 keV. The largest energy observed is 2.3 keV. With $E_\parallel = 6 \times 10^5\ \mathrm{V\ m^{-1}}$ and $\delta = 0.4$ cm, the observed electron final kinetic energy agrees with our expected energy, i.e., $\Delta K = E_\parallel \delta = 2.4$ keV. While highly simplified, this particle simulation nevertheless indicates that high-energy X-rays could come from the electric field generated by the KDRT-induced magnetic reconnection; it thus gives insight into the acceleration process creating high-energy electrons. This description of the electron acceleration process is very simplified and macroscopic; a more physically realistic description that takes into account changes in collisionality of electrons as they accelerate was given in Marshall & Bellan (2019).

6. Discussion

The camera enables a much better estimate of the jet radius than magnetic probes because the camera has 10 times better spatial resolution than magnetic probes (1 mm resolution for camera versus 10 mm for the available probes). In the past (Zhai et al. 2014), the actual magnetic radii of the jets were believed to be larger than the visible images shown in Figure 1 (a = 3–5 cm). However, the result of the 3D simulation here suggests that the jet radius might be closer to the observed radius from the visible light emission than previously presumed. For a plasma jet with an azimuthal magnetic field $B_\theta = 1.9$ T and a minor radius $a = 1 \pm 0.25$ cm, the corresponding axial current is $I = 2\pi a B_\theta/\mu_0 = 95 \pm 24$ kA. For this same shot, Moser & Bellan (2012) reported a consistent peak current of $I = 110$ kA. Furthermore, a recent study of magnetic RTI by Zhang et al. (2020) on the arched plasma loop experiment with similar parameters (a, $\lambda_{RT} = 1$ cm and $\kappa T = 2$ eV) also supports that the expected minor radius is close to the observation from the images, $a \sim 1$ cm. Both in that study and here, the observed RTI is magnetized and driven by the effective gravity associated with a strong lateral acceleration. An accurate measure of the jet radius will be important for the future study of this phenomenon; conversely, by understanding its physical mechanism, knowing plasma dynamics and density allows us to estimate the plasma jet radius.

Many models of the solar corona are based on the zero-β approximation and yet describe the corona in terms of the evolution of reconnecting magnetic fields. A zero-β code is only able to capture the current-driven instability but not the pressure-driven one. Although a path to the reconnection scale

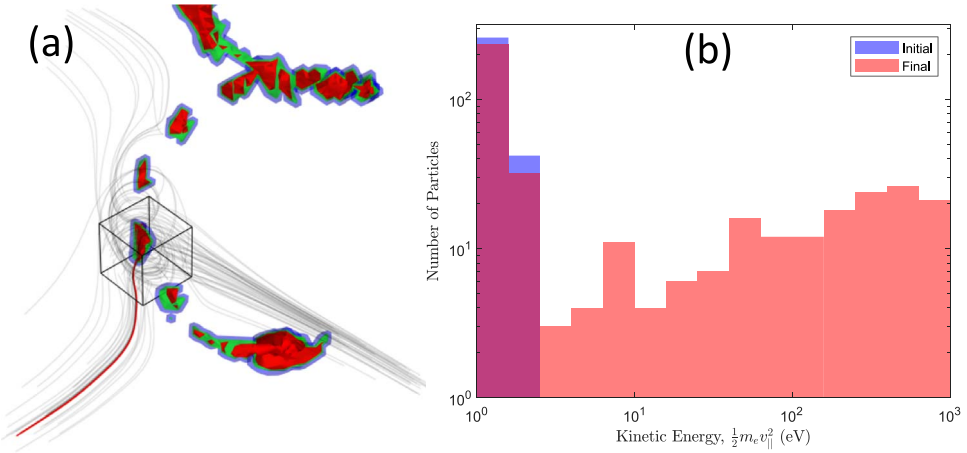

Figure 5. (a) Isosurfaces of $E_{||} = \eta \boldsymbol{J} \cdot \boldsymbol{B}/B$. The colors green, blue, and red represent the levels {0.1, 0.4, 0.6} of the maximum value of this time step, respectively. The gray lines shows 100 random particle trajectories. The red lines shows the trajectory of the highly accelerated particles. The cube indicates the domain of the initial position. (b) Distribution of the test particles' initial and final energies.

by only current-driven instability exists, it disregards the possibility of fast reconnection due to pressure-driven instability. For example, Seo et al. (2020) observed a cascade progression sequence from sausage-like pinching to KI that leads to fast reconnection in a different regime of the same Caltech jet experiment. In order to take into account the possible role that KDRT might play in fast reconnection and particle energization in the solar corona, it would be worthwhile to extend the reconnection model to include finite-β, collimation physics with associated paramagnetism, the d_i scale, and anomalous resistivity associated with localized high current density.

In summary, the experimentally observed cascade of instabilities from KI to RTI was simulated using a resistive MHD code. We found that (1) spatial localization (paramagnetism) of B_z is crucial to achieve the KDRT, (2) the dependence on Φ^2 given in Zhai & Bellan (2016) was verified, and (3) electrons can be accelerated to high energy through this process.

This work was supported by NSF/DOE Partnership in Plasma Science and Engineering under award DE-FG02-04ER54755 and AFOSR under award FA9550-11-1-0184. H. L. acknowledges support from the DOE/OFES and LANL/LDRD programs.

ORCID iDs

Pakorn Wongwaitayakornkul https://orcid.org/0000-0001-7455-8582
Hui Li https://orcid.org/0000-0003-3556-6568
Paul M. Bellan https://orcid.org/0000-0002-0886-8782

References

Bellan, P. M. 2018a, PhPl, 25, 055601
Bellan, P. M. 2018b, JPlPh, 84, 755840501
Bergerson, W., Forest, C., Fiksel, G., et al. 2006, PhRvL, 96, 015004
Bernstein, I. B., Frieman, E., Kruskal, M. D., & Kulsrud, R. 1958, RSPSA, 244, 17
Carlyle, J., Williams, D. R., van Driel-Gesztelyi, L., et al. 2014, ApJ, 782, 87
Chai, K.-B., Zhai, X., & Bellan, P. M. 2016, PhPl, 23, 032122
Chen, L., & Wu, D. 2012, ApJ, 754, 123
Drake, J., Shay, M., & Swisdak, M. 2008, PhPl, 15, 042306
Eyink, G. L., Lazarian, A., & Vishniac, E. T. 2011, ApJ, 743, 51
Furth, H. P., Killeen, J., & Rosenbluth, M. N. 1963, PhFl, 6, 459
Goedbloed, H., Keppens, R., & Poedts, S. 2019, Magnetohydrodynamics: Of Laboratory and Astrophysical Plasmas (Cambridge: Cambridge Univ. Press)
Haw, M. A., Seo, B., & Bellan, P. M. 2019, GeoRL, 46, 7105
Hsu, S. C., & Bellan, P. M. 2003, PhRvL, 90, 215002
Klimchuk, J. 2001, SoPh, 193, 53
Kruskal, M. D., Johnson, J., Gottlieb, M., & Goldman, L. 1958, PhFl, 1, 421
Kruskal, M. D., & Schwarzschild, M. 1954, RSPSA, 223, 348
Kumar, D., & Bellan, P. M. 2009, PhRvL, 103, 105003
Li, S., & Li, H. 2003, Los Alamos National Lab, Tech. Rep. LA-UR-03-8926
Li, X., & Cross, R. 1994, RScI, 65, 2623
Linton, M., Longcope, D., & Fisher, G. 1996, ApJ, 469, 954
Marshall, R., & Bellan, P. 2019, PhPl, 26, 042102
Marshall, R., Flynn, M., & Bellan, P. 2018, PhPl, 25, 112101
Moser, A. L., & Bellan, P. M. 2012, Natur, 482, 379
Northrop, T. G. 1961, AnPhy, 15, 79
Parker, E. N. 1957, JGR, 62, 509
Strutt, J. W. 1883, in Proceedings of the London Mathematical Society, 14, 170
Rust, D., & LaBonte, B. 2005, ApJL, 622, L69
Seo, B., Wongwaitayakornkul, P., Haw, M. A., et al. 2020, PhPl, 27, 022109
Shafranov, V. 1958, JETP, 6, 1013
Suydam, B. R. 1958, JNuE, 7, 275
Sweet, P. A. 1958, in IAU Symp. 6, Electromagnetic Phenomena in Cosmical Physics, ed. B. Lehnert (Cambridge: Cambridge University Press), 499
Taylor, G. I. 1950, RSPSA, 201, 192
Török, T., & Kliem, B. 2005, ApJL, 630, L97
Wilkins, M. L. 1980, JCoPh, 36, 281
Wongwaitayakornkul, P., Haw, M. A., Li, H., Li, S., & Bellan, P. M. 2017, ApJ, 848, 89
Yamada, M., Kulsrud, R., & Ji, H. 2010, RvMP, 82, 603
Yoon, Y. D., & Bellan, P. M. 2019, PhPl, 26, 100702
Youngs, D. L. 1984, PhyD, 12, 32
Youngs, D. L. 1991, PhFl, 3, 1312
Yun, G. S., & Bellan, P. M. 2010, PhPl, 17, 062108
Zhai, X., & Bellan, P. M. 2016, PhPl, 23, 032121
Zhai, X., Li, H., Bellan, P. M., & Li, S. 2014, ApJ, 791, 40
Zhang, Y., Wongwaitayakornkul, P., & Bellan, P. M. 2020, ApJL, 889, L32